Radiometrically Calibrated Features of Full-Waveform Lidar Point Clouds Based on Statistical Moments

Andreas Roncat, Christian Briese, Josef Jansa, and Norbert Pfeifer

***Abstract*—Full-waveform lidar has gained increasing attention in 3-D remote sensing and related disciplines during the last decade due to its capability of delivering both geometric and radiometric information in the same spatial resolution. Radiometric information may either be related to the echo, e.g., echo amplitude and width, or to the target itself, e.g., the backscatter cross section (BCS). Echo parameters, often obtained by Gaussian decomposition, as well as target properties, which are (geo)physical properties and therefore independent of data acquisition mission parameters, are considered as additional features of the point cloud generated by laser scanning. The BCS commonly is derived by performing a deconvolution which results in its temporal derivative, the differential backscatter cross-section (dBCS), and subsequent integration. The temporal shape of the dBCS has gained little attention in the literature so far. In this letter, we discuss the derivation of additional *target* parameters, namely the statistical moments of the respective target dBCS. Besides discussing the applicability of established deconvolution approaches for the extraction of statistical moments in the dBCS, special emphasis is laid on their derivation in B-spline-based deconvolution. Uniform B-splines allow for linear deconvolution and subsequent radiometric calibration. We illustrate the potential of the proposed method by a sample data set stemming from an airborne lidar campaign in complex mountainous terrain.**

***Index Terms*—Deconvolution, differential backscatter cross-section (dBCS), feature extraction, laser scanning, light detection and ranging (lidar).**

I. Introduction and Motivation

THE use and demand for 3-D topographic data have seen an ongoing increase in the past years. Airborne lidar (light detection and ranging), also referred to as airborne laser scanning (ALS), has played a leading role. Its results, from the raw 3-D point clouds to subsequently derived digital models, have been in use in many scientific and application areas, such as hydrology [1], [2], archaeology [3], forestry [4], geomorphology [5], 3-D city modeling [6], [7], detection and reconstruction of power lines [8].

Special ALS instruments, capable of *full-waveform* (FWF) digitization, enable for the extraction of both geometric and radiometric information in the same spatial resolution. Discrete-return systems deliver a limited number of echoes per laser shot, possibly accompanied by an intensity value, given as a unitless digital number. In contrast, FWF systems allow for the extraction of a higher number of echoes, especially in short distances to each other [9]. Furthermore, radiometric quantities of an echo such as amplitude and echo width can be computed. Full-waveform digitization performs an analog-to-digital conversion of the incoming signal with a sampling in the order of 1 ns. In comparison to single-photon-counting systems or gated viewing, both relying on multiple shots to synthesize the histograms (waveforms) of the target's backscatter [10], the raw waveforms studied here are smoother. An introduction to small-footprint FWF lidar, as dealt with in this letter, is given in [11] and [12].

Mallet *et al.* [13] derived *echo* attributes by assigning a function class to an echo and calculating the function parameters for best fit. However, these *echo* attributes alone do not allow a physical interpretation of the *target* since they are dependent on the temporal profile and variability of the outgoing laser pulse as well as on the settings of the flight mission (e.g., altitude, pulse repetition rate and scan angle).

A further approach for such purposes is Gaussian Decomposition which enables for additional radiometric calibration of the FWF data [11], [14]. Gaussian Decomposition allows for implicit deconvolution and thus determination of the differential backscatter cross-section (dBCS) as a spatially variable physical target attribute. However, the approach relies on the symmetry of both the outgoing laser pulse and the scattering characteristics of the targets and so far, mainly echo attributes have been derived from the echo waveform and used for classification tasks, e.g., by using the echo width for classification of ground points [15].

This letter uses B-spline deconvolution [16] as basis. Radiometric calibration in this context is described in [17] which allows physical units to be given to all derived target properties. Our contributions are:

1) radiometric calibration integrated in B-Spline deconvolution which does not make symmetry and temporal stability assumptions;

Manuscript received April 1, 2013; revised July 1, 2013 and July 18, 2013; accepted July 19, 2013. Date of publication August 27, 2013; date of current version November 25, 2013. The work of the first author was supported by a Karl Neumaier Ph.D. scholarship. The Ludwig Boltzmann Institute for Archaeological Prospection and Virtual Archaeology is based on an international cooperation of the Ludwig Boltzmann Gesellschaft (Austria) with various international partners. The authors were supported by the COMET project MUSICALS (MUltiscale Snow/ICemelt Discharge Simulation into ALpine ReservoirS) and C4Austria (Climate Change Consequences for the Cryosphere) funded by the Austrian Climate Research Program (ACRP).

A. Roncat, J. Jansa, and N. Pfeifer are with the Research Groups Photogrammetry and Remote Sensing, Department of Geodesy and Geoinformation, Vienna University of Technology, 1040 Vienna, Austria (e-mail: andreas.roncat@geo.tuwien.ac.at; josef.jansa@geo.tuwien.ac.at; norbert.pfeifer@geo.tuwien.ac.at).

C. Briese is with the Research Groups Photogrammetry and Remote Sensing, Department of Geodesy and Geoinformation, Vienna University of Technology, 1040 Vienna, Austria and also with the Ludwig Boltzmann Institute for Archaeological Prospection and Virtual Archaeology, 1190 Vienna, Austria (e-mail: christian.briese@geo.tuwien.ac.at).

Color versions of one or more of the figures in this paper are available online at http://ieeexplore.ieee.org.

Digital Object Identifier 10.1109/LGRS.2013.2274557

2) practical demonstration of FWF point-cloud derivation based on the first statistical moments (means) of the dBCS; and
3) analysis of the central higher order moments (second to fourth order) of the dBCS.

The letter is organized as follows: Section II is focused on the physical background and the retrieval of the dBCS $\sigma'(t)$ and its integral, the backscatter cross-section (BCS) σ using uniform B-splines. The proposed approach for extraction of discrete targets and radiometrically calibrated attributes from the dBCS is presented in Section III. In the subsequent section, a sample data set, recorded over complex mountainous terrain in the Ötztal Alps (Tyrol, Austria) is presented and discussed to illustrate the potential of the presented approach. Conclusions are given in Section V.

II. Theory

The radar equation relates the *transmitted* laser power $P_t(t)$ of a single laser pulse to the corresponding *echo* power $P_e(t)$ [18]

$$P_e(t) = \frac{D_r^2}{4\pi R^4 \beta_t^2} P_t\left(t - \frac{2R}{v_g}\right) \sigma \eta_S \eta_A \tag{1}$$

with β_t denoting the beamwidth of the transmitted signal, R the distance from the sensor to the target, t the travel time, v_g the group velocity of the laser ray, σ the effective BCS (in m^2), D_r the receiving aperture diameter, η_A the atmospheric transmission factor, and η_S the system transmission factor. The BCS is a product of the target area $(A[\mathrm{m}^2])$, the target reflectivity $(\varrho[\,])$, and the factor $4\pi/\Omega$ describing the scattering angle of the target $(\Omega[\mathrm{sr}])$ in relation to an isotropic scatterer [18]: $\sigma = (4\pi\varrho A)/\Omega$.

The ability to differentiate two scatterers along the line of sight is limited by the digitization interval and the width of the transmitted laser pulse. Equally reflective targets which are closer to each other than half the pulse width do not result in separate maxima in the echo waveform. However, using advanced signal processing, the separation of targets closer than half the pulse width is still possible [9]. Even shorter separations were reported in [10] where the dBCS was a set of Dirac impulses, thus making more assumptions on the observed scene. Below the actual minimum separation distance, subsequent targets form an inseparable cluster, regarded as single scatterers each. This gives a simplified version of $P_e(t)$ as sum of the contributions of N distinct scatterers

$$P_e(t) = \sum_{i=1}^{N} \frac{D_r^2}{4\pi R_i^4 \beta_t^2} \eta_S \eta_A P_t(t) \otimes \sigma_i'(t) \tag{2}$$

with "$\otimes$" denoting the convolution operator. Both the transmitted signal and the received echo travel through the signal processing chain of the scanner, therefore $P_t(t)$ and $P_e(t)$ cannot be observed directly. However, one can observe their convolution with the system response $\Gamma(t)$ of the instrument. This convolution results in the *system waveform* $S(t) = P_t(t) \otimes \Gamma(t)$ and the *recorded echo power* $P_r = P_e(t) \otimes \Gamma(t)$, respectively.

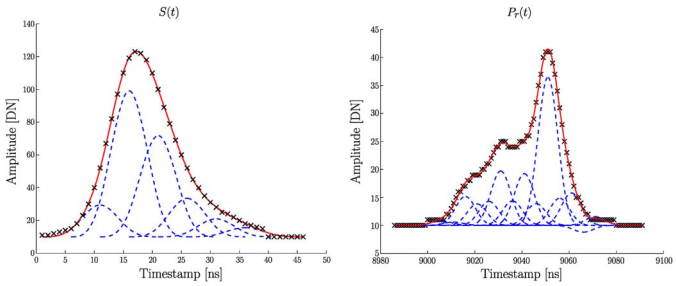

Fig. 1. System waveform $S(t)$ and recorded echo waveform $P_r(t)$ modeled as uniform B-spline curves. The original sampled values are indicated by black crosses.

Using the commutativity of the convolution operator, the radar equation can be written as follows:

$$P_r(t) = \sum_{i=1}^{N} \frac{D_r^2}{4\pi R_i^4 \beta_t^2} \eta_S \eta_A S(t) \otimes \sigma_i'(t). \tag{3}$$

The BCS σ_i of a target i is the integral of the dBCS $\sigma_i'(t)$

$$\sigma_i = \int_{-\infty}^{\infty} \sigma_i'(t)\, dt. \tag{4}$$

Though being a physical property of the scatterer, σ depends on the incidence angle of the laser beam to the scattering surface and the effective illuminated area A of this scatterer, and of course on the wavelength of the laser used to illuminate the target [17], [19].

A. B-Spline Deconvolution and Radiometric Calibration

Using uniform B-splines, the the BCS σ can be reconstructed as follows [17]:

1) modeling of $S(t)$ and $P_r(t)$ as continuous functions with uniform B-splines;
2) deconvolution of $P_r(t)$ by $S(t)$, yielding again a uniform B-spline curve;
3) formulation and determination of a calibration constant C_{CAL} containing the constant but (yet) unknown parameters in the radar equation;
4) application of C_{CAL} to finally derive the dBCS and the BCS.

Beginning with the formulation of $S(t)$ and $P_r(t)$ as continuous functions, we retrieve [16]

$$S(t) = \sum_{i=1}^{i_{\max}} b_{i,\varepsilon} B_i^{n_\varepsilon}(t) \qquad P_r(t) := \sum_{k=1}^{k_{\max}} b_{k,\rho} B_k^{n_\rho}(t) \tag{5}$$

with the B_i^n being uniform B-splines, i.e., piecewise continuous polynomial functions, scaled by the parameters (control points) $b_{i,\varepsilon}$ and $b_{k,\rho}$, respectively. An example for modeling $S(t)$ and $P_r(t)$ as uniform B-spline curves is given in Fig. 1. The knot distance Δt between subsequent control points and the degrees n_ε and n_ρ need to be set in advance.

For deconvolution—denoted by the symbol "$\otimes^{-1}$"—we introduce a "distorted" version of the dBCS

$$\bar{\sigma}'(t) = \frac{D_r^2 \eta_S \eta_A}{4\pi R^4 \beta_t^2}\, \sigma'(t) = P_r(t) \otimes^{-1} S(t). \tag{6}$$

Note that the above equation does not refer to a single scatterer but to the deconvolution of the whole backscattered waveform; it is a uniform B-spline curve of degree $n_\sigma = n_\rho - n_\varepsilon - 1$ and $j_{\max} = k_{\max} - i_{\max} + 1$ control points $b_{j,\sigma}$.

For retrieving $\bar{\sigma}'(t)$ with using B-spline deconvolution, we have to solve the overdetermined linear equation system

$$b_{k,\rho} = \sum_{i,j:i+j-1=k} b_{i,\varepsilon} b_{j,\sigma} \tag{7}$$

with the control points $b_{j,\sigma}$ of $\bar{\sigma}'(t)$ as unknowns [16], which follows from the properties of B-splines under convolution. In contrast, Gaussian Decomposition allows for solving the deconvolution implicitly [17].

We can extract from (6) the terms β_t, D_r, η_S, and η_A as unknown, but constant parameters. We finally get as *calibration constant* C_{CAL}

$$C_{\mathrm{CAL,B}} = \frac{4\pi\beta_t^2}{\eta_S \eta_A D_r^2} \tag{8}$$

where the index $_B$ denotes the B-spline approach. (The formulation of C_{CAL} for Gaussian Decomposition is slightly different, cf. [20].) The unit of $C_{\mathrm{CAL,B}}$ is m^{-2}. Empirical studies have shown that the stability of the system waveform is not sufficiently given [21], [22]. Thus, in our approach every recorded echo waveform is deconvolved by its corresponding system waveform. The calibration constant is determined using either reflectivity assumptions in homogeneous areas [11], natural [23] or artificial [24] reference targets.

The range influence in the deconvolution can be eliminated by multiplying each B-spline j with its mean range $R_{j,\mathrm{mean}}$ to the power of 4, so every base function $B_j^{n_\sigma}$ is scaled by an individual, but known factor $\tilde{b}_{j,\sigma}$ [17]

$$\tilde{\sigma}'(t) := \sum_{j=1}^{j_{\max}} \underbrace{R_{j,\mathrm{mean}}^4 b_{j,\sigma}}_{=:\tilde{b}_{j,\sigma}} B_j^{n_\sigma} = \frac{\eta_S \eta_A D_r^2}{4\pi\beta_t^2}\, \sigma'(t).$$

With the above results for range determination of single B-spline elements and the solution for C_{CAL}, we can formulate the dBCS as

$$\sigma'(t) = C_{\mathrm{CAL,B}}\, \tilde{\sigma}'(t) \tag{9}$$

and consequently its integral σ as [17]

$$\sigma = C_{\mathrm{CAL,B}} \int_{-\infty}^{\infty} \tilde{\sigma}'(t)\, dt = C_{\mathrm{CAL,B}} \Delta t \sum_{j=1}^{j_{\max}} \tilde{b}_{j,\sigma}. \tag{10}$$

It shall be stated once again that still no discrete targets have been extracted up to this point but the dBCS has been formulated as a continuous function along the laser's line of sight. The extraction of individual echoes and target parameter determination, both performed by calculating the statistical moments, will be presented in the subsequent section.

B. Statistical Moments of the dBCS

A univiariate function $f(x)$ can be considered as a probability density function if $f(x) \geq 0$ for all x and its integral equals 1. For such functions, statistical moments are defined as given below. Provided that the dBCS of a target is non-negative, a physical necessity, its fist statistical moment of $\sigma_i'(t)$, the mean $m_{1,i}$, is defined as

$$m_{1,i} := \frac{1}{\int_{-\infty}^{\infty} \sigma_i'(t)\, dt} \int_{-\infty}^{\infty} t\sigma_i'(t)\, dt = \frac{1}{\sigma_i} \int_{-\infty}^{\infty} t\sigma_i'(t)\, dt. \tag{11}$$

The *central* moments of degree n ($n > 1$) are defined as

$$\overline{m}_{n,i} := \frac{1}{\sigma_i} \int_{-\infty}^{\infty} (t - m_{i,1})^n \sigma_i'(t)\, dt. \tag{12}$$

The second central moment $\overline{m}_{2,i}$ is referred to as variance, its square root as standard deviation. We will concentrate on the central moments of degree 2 to 4 in the subsequent text.

In the case of discrete functions, the integral is to be replaced by a sum. The statistical moments of B-spline curves can be derived analytically since these curves consist of piecewise continuous polynomial functions.

III. Method

In this section, we describe the determination of the number of targets in a dBCS derived by B-spline deconvolution, the localization and subsequent derivation of target features from the central moments of higher order. The dBCS is a piecewise continuous univariate polynomial of low degree (typically 2 or 3 [16], [17]), so that its roots, derivatives and integral can be calculated analytically. The number of targets is calculated by extracting local minima in the dBCS from roots of its first derivative. It results to the number of local minima minus 1. The positions of the ith and $(i+1)$th minimum are taken as lower and upper bound $t_{l,i}$ and $t_{u,i}$ of a dBCS segment contributing to a target i, with $t_{l,i+1} = t_{u,i}$. The corresponding segment $\sigma_i'(t)$ is defined as $\sigma_i'(t) := \sigma'(t)$ for $t \in [t_{l,i}, t_{u,i})$ and 0 elsewhere. Its integral σ_i gives the BCS of the ith target. In analogy to Gaussian Decomposition, the mean $m_{1,i}$ is taken as the location of this target. The central moments of higher degree are calculated using the formulas given in Section II-B. Fig. 2 shows an example for this procedure, stemming from an ALS data set recorded with an Optech ALTM 3100 system.

Due to noise, small negative parts may appear in the dBCS. Since such negative parts contradict both the underlying physical model and the prerequisites for a probability density function, these parts are eliminated from further analysis and their minimum replaced by the roots of the dBCS next to it.

A. Statistical Moments of the dBCS in Other Deconvolution Approaches in Lidar Research

Gaussian decomposition [11] aims at reconstructing the echo signal as superposition of Gaussian functions, i.e., scaled normal distributions. Since the system waveform is a Gaussian,

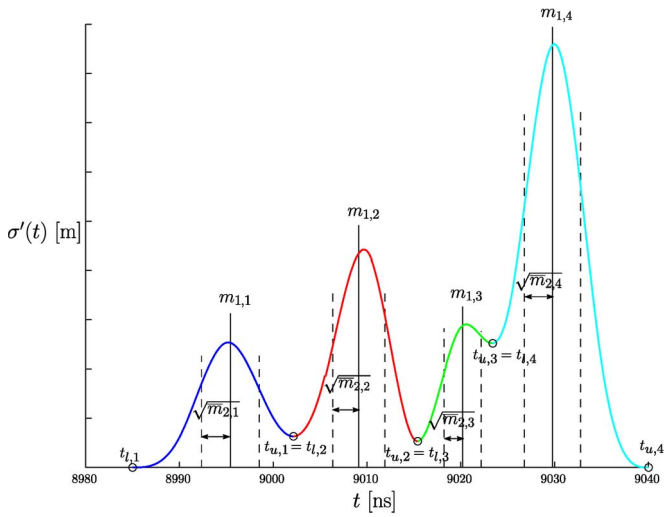

Fig. 2. Example for target extraction and localization and feature derivation based on statistical moments of the dBCS. The target location is set to the mean $m_{1,i}$ of the segment between the ith and $(i+1)$th local minimum; its BCS is the area under the curve in this segment. The image further shows the square roots of the second central moments (variances), the standard deviations $\sqrt{m_{2,i}}$.

the output of the deconvolution results to a Gaussian. Normal distributions are fully characterized by their first (mean) and second central moment (variance), so that the higher moments do not contain further information.

EM-Deconvolution [25] is targeted at deconvolving the echo waveform by the system waveform into a train of spikes (one per target) in a discrete time series. Thus, no statistical moments besides the mean can be derived from the deconvolution.

Wiener-Filter [26] and regularized least-squares deconvolution [27] reconstruct the dBCS by discrete deconvolution in time domain and spectra division in the frequency domain, resp. Moments of arbitrary order can be derived from the resulting function which is a discrete function though. In [26], the deconvolution is eventually fitted to a superposition of Gaussian functions, which makes assumptions on the dBCS.

IV. Results and Discussion

The presented approach was investigated using FWF and discrete-return ALS data from a flight strip within a campaign performed in the Ötztal Alps (Tyrol, Austria) in October 2010. In this campaign, an Optech ALTM 3100 instrument was used, operating at a wavelength of 1064 nm, a pulse repetition rate of 70 kHz and a pulse width of approximately 10 ns [12], [28]. With a beam divergence of 0.3 mrad and maximum range of 2 km, the maximal footprint size was 0.6 m. We chose our test site around the village Obergurgl where built-up areas, open terrain, high and low vegetation were present, as well as flat areas and steep slopes (see Fig. 3). The 3-D point cloud (approximately 1 pt/m^2) was calculated from the extracted means in the dBCS segments and the direct georeferencing information.

The distributions of the BCS and the central moments from degree 2 to 4 show a clear bimodality for the variance and the fourth moment which are apparently quadratically dependent (see Fig. 4). Visual analysis of Fig. 5 and the orthophoto in

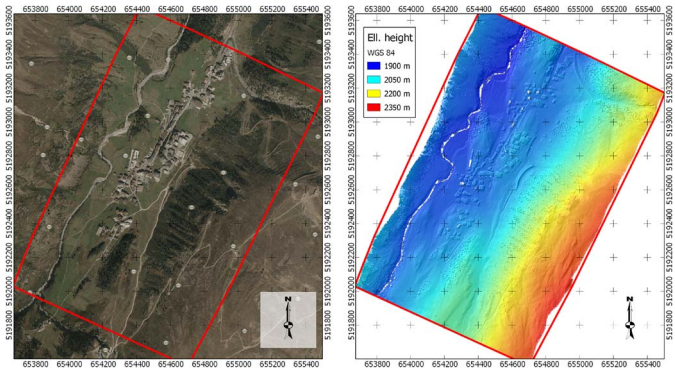

Fig. 3. (Left) Orthophoto of the test area in Obergurgl (Tyrol, Austria). Orthophoto: www.geoimage.at, accessed on July 18, 2013. (Right) Digital surface model of the test area. Coordinates given in UTM, Zone 32N.

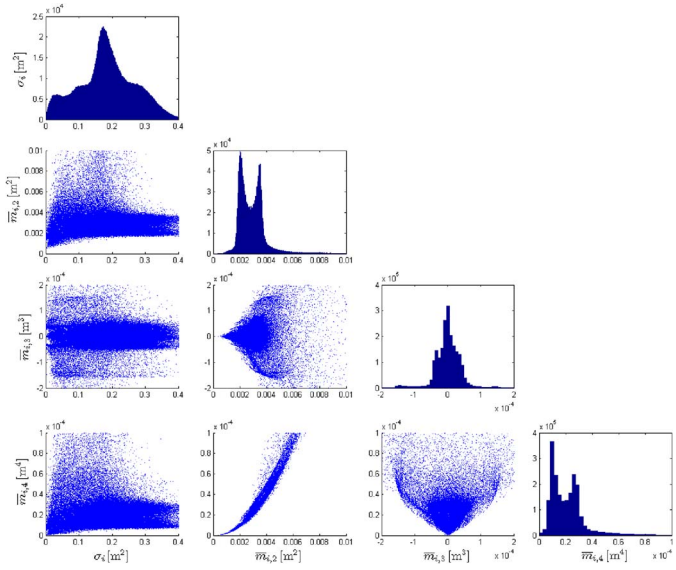

Fig. 4. Distributions of the parameters extracted from the test data set (cf. Fig. 3): Histograms of the BCS σ_i and the second to fourth central moments of its derivative, $\overline{m}_{i,2..4}$ (diagonal, from top to bottom). The non-diagonal diagrams show the scatter plots of two of the four variables. The quadratic relationship of $\overline{m}_{i,2}$ and $\overline{m}_{i,4}$ is clearly visible.

Fig. 3 suggests that the combination of BCS and variance may enable discrimination between the following landcover classes; see Fig. 5):

- built-up areas: very low BCS, low variance;
- sparse alpine vegetation: low BCS, low variance;
- high vegetation: low BCS, high variance;
- grassland: high BCS, low variance.

The third-order moments did only show additional information in the way that positive values (and thus, positive skewness) appeared mainly in higher vegetation. Consequently, these moments were not investigated further.

Moreover, we analysed the geometric performance of the presented approach in comparison to the discrete-return point cloud and an FWF point cloud extracted with Gaussian decomposition of the same flight strip in smooth areas. The B-spline-derived ranges tend to be a few centimeters (mean: 2.5 cm, $\sigma_{\mathrm{MAD}} = 2$ cm) lower than the corresponding ones of the sensor and of Gaussian Decomposition.

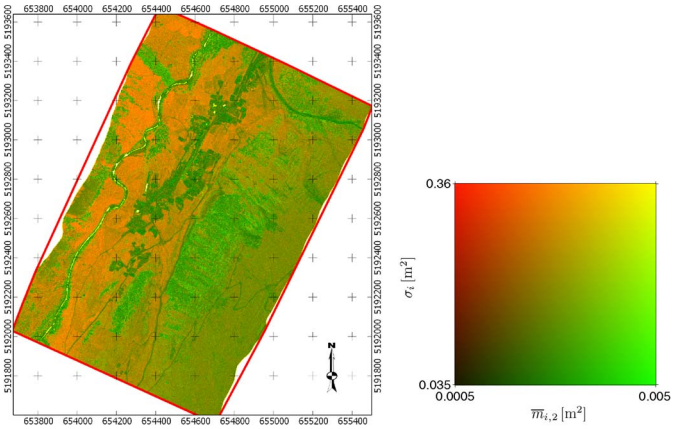

Fig. 5. Top view of the ALS point cloud of the test area (cf. Fig. 3). While the point locations stem from the first statistical moments of the dBCS segments, the color coding is composed of the BCS σ_i (red channel) and the variance of the dBCS $\overline{m}_{i,2}$ (green channel).

V. Conclusion

This letter presents a novel approach for calculating target features in full-waveform lidar data, derived by a B-spline-based approach for deconvolution and radiometric calibration. The mentioned features, stemming from the dBCS, are the statistical moments of the dBCS, whose temporal profile had not received the appropriate attention in the literature so far. The first moment, i.e., the mean, serves for locating the target in space, whereas the central moments of higher order can be regarded as radiometrically calibrated point features. On behalf of a data set recorded in complex alpine terrain, it was shown that the derived point cloud is comparable to both a discrete-return point cloud as well as to a full-waveform point cloud derived by Gaussian Decomposition. Moreover, especially the second and fourth central moments, in combination with the BCS, have shown their potential for separation of different landcover types. Future research will focus on enhanced 3-D classification using the statistical moments and, on the algorithmic side, regularizing the used approach in order so suppress noise.

Acknowledgment

The authors gratefully acknowledge the efforts of the anonymous reviewers to improve the quality of this letter.

References

[1] D. M. Cobby, D. C. Mason, and I. J. Davenport, "Image processing of airborne scanning laser altimetry data for improved river flood modelling," *ISPRS J. Photogramm. Remote Sens.*, vol. 56, no. 2, pp. 121–138, Dec. 2001.

[2] G. Mandlburger, C. Hauer, B. Höfle, H. Habersack, and N. Pfeifer, "Optimisation of LiDAR derived terrain models for river flow modelling," *Hydrol. Earth Syst. Sci.*, vol. 13, no. 8, pp. 1453–1466, Aug. 2009.

[3] M. Doneus, C. Briese, M. Fera, and M. Janner, "Archaeological prospection of forested areas using full-waveform airborne laser scanning," *J. Archaeol. Sci.*, vol. 35, no. 4, pp. 882–893, Apr. 2008.

[4] E. Nsset and T. Gobakken, "Estimating forest growth using canopy metrics derived from airborne laser scanner data," *Remote Sens. Environ.*, vol. 96, no. 3/4, pp. 453–465, Jun. 2005.

[5] B. Höfle and M. Rutzinger, "Topographic airborne LiDAR in geomorphology: A technological perspective," *Zeitschrift Geomorphol./Ann. Geomorphol.*, vol. 55, no. S2, pp. 1–29, Apr. 2011.

[6] G. Zhou, C. Song, J. Simmers, and P. Cheng, "Urban 3D GIS from LiDAR and digital aerial images," *Comput. Geosci.*, vol. 30, no. 4, pp. 345–353, May 2004.

[7] P. Dorninger and N. Pfeifer, "A comprehensive automated 3D approach for building extraction, reconstruction, and regularization from airborne laser scanning point clouds," *Sensors*, vol. 8, no. 11, pp. 7323–7343, Nov. 2008.

[8] M. Ritter and W. Benger, "Reconstructing power cables from lidar data using eigenvector streamlines of the point distribution tensor field," *J. WSCG*, vol. 20, no. 3, pp. 223–230, 2012.

[9] C. E. Parrish, I. Jeong, R. D. Nowak, and R. Brent Smith, "Empirical comparison of full-waveform lidar algorithms: Range extraction and discrimination performance," *Photogramm. Eng. Remote Sens.*, vol. 77, no. 8, pp. 825–838, Aug. 2011.

[10] S. Hernández-Marín, A. M. Wallace, and G. J. Gibson, "Bayesian analysis of lidar signals with multiple returns," *IEEE Trans. Pattern Anal. Mach. Intell.*, vol. 29, no. 12, pp. 2170–2180, Dec. 2007.

[11] W. Wagner, A. Ullrich, V. Ducic, T. Melzer, and N. Studnicka, "Gaussian decomposition and calibration of a novel small-footprint full-waveform digitising airborne laser scanner," *ISPRS J. Photogramm. Remote Sens.*, vol. 60, no. 2, pp. 100–112, Apr. 2006.

[12] C. Mallet and F. Bretar, "Full-waveform topographic lidar: State-of-the-art," *ISPRS J. Photogramm. Remote Sens.*, vol. 64, no. 1, pp. 1–16, Jan. 2009.

[13] C. Mallet, F. Lafarge, M. Roux, U. Soergel, F. Bretar, and C. Heipke, "A marked point process for modeling lidar waveforms," *IEEE Trans. Image Process.*, vol. 19, no. 12, pp. 3204–3221, Dec. 2010.

[14] M. Hofton, J. Minster, and J. Blair, "Decomposition of laser altimeter waveforms," *IEEE Trans. Geosci. Remote Sens.*, vol. 38, no. 4, pp. 1989–1996, Jul. 2000.

[15] Y.-C. Lin, J. Mills, and S. Smith-Voysey, "Rigorous pulse detection from full-waveform airborne laser scanning data," *Int. J. Remote Sens.*, vol. 31, no. 5, pp. 1303–1324, Feb. 2010.

[16] A. Roncat, G. Bergauer, and N. Pfeifer, "B-spline deconvolution for differential target cross-section determination in full-waveform laser scanner data," *ISPRS J. Photogramm. Remote Sens.*, vol. 66, no. 4, pp. 418–428, Jul. 2011.

[17] A. Roncat, N. Pfeifer, and C. Briese, "A linear approach for radiometric calibration of full-waveform Lidar data," in *Proc. SPIE 8537, Image Signal Process. Remote Sens. XVIII*, 2012, pp. 853 708-1–853 708-12.

[18] A. V. Jelalian, *Laser Radar Systems*. Boston, MA, USA: Artech House, 1992.

[19] H. Lehner and C. Briese, "Radiometric calibration of full-waveform airborne laser scanning data based on natural surfaces," in *Proc. Int. Arch. Photogramm., Remote Sens. Spatial Inf. Sci. 38 (Part 7B)*, Vienna, Austria, 2010, pp. 360–365.

[20] W. Wagner, "Radiometric calibration of small-footprint full-waveform airborne laser scanner measurements: Basic physical concepts," *ISPRS J. Photogramm. Remote Sens.*, vol. 65, no. 6, pp. 505–513, Nov. 2010.

[21] F. Bretar, A. Chauve, J.-S. Bailly, C. Mallet, and A. Jacome, "Terrain surfaces and 3-D landcover classification from small footprint full-waveform lidar data: Application to badlands," *Hydrol. Earth Syst. Sci.*, vol. 13, no. 8, pp. 1531–1545, Aug. 2009.

[22] A. Roncat, H. Lehner, and C. Briese, "Laser pulse variations and their influence on radiometric calibration of full-waveform laser scanner data," in *Proc. Int. Arch. Photogramm., Remote Sens. Spatial Inf. Sci. 38 (Part 5/W12)*, 2011, pp. 137–142.

[23] C. Briese, B. Höfle, H. Lehner, W. Wagner, and M. Pfenningbauer, "Calibration of full-waveform airborne laser scanning data for object classification," in *Proc. SPIE, Laser Radar Technol. Appl. XIII*, 2008, pp. 69500H-1–69500H-8.

[24] S. Kaasalainen, H. Hyyppä, A. Kukko, P. Litkey, E. Ahokas, J. Hyyppä, H. Lehner, A. Jaakkola, J. Suomalainen, A. Akujarvi, M. Kaasalainen, and U. Pyysalo, "Radiometric calibration of lidar intensity with commercially available reference targets," *IEEE Trans. Geosci. Remote Sens.*, vol. 47, no. 2, pp. 588–598, Feb. 2009.

[25] C. E. Parrish and R. D. Nowak, "Improved approach to lidar airport obstruction surveying using full-waveform data," *J. Eng. Survey.*, vol. 135, no. 2, pp. 72–82, May 2009.

[26] B. Jutzi and U. Stilla, "Range determination with waveform recording laser systems using a Wiener filter," *ISPRS J. Photogramm. Remote Sens.*, vol. 61, no. 1, pp. 95–107, Nov. 2006.

[27] Y. Wang, J. Zhang, A. Roncat, C. Künzer, and W. Wagner, "Regularizing method for the determination of the backscatter cross section in lidar data," *J. Opt. Soc. Amer. A, Opt. Image Sci.*, vol. 26, no. 5, pp. 1071–1079, May 2009.

[28] L. Chasmer, C. Hopkinson, B. Smith, and B. Treitz, "Examining the influence of changing laser pulse repetition frequencies on conifer forest canopy returns," *Photogramm. Eng. Remote Sens.*, vol. 72, no. 12, pp. 1359–1367, Dec. 2006.